A Diffusion Model for Multi-Layered Metasurface Unit Cell Synthesis

CHEN NIU (Graduate Student Member, IEEE), **MARIO PHANEUF** (Graduate Student Member, IEEE),
AND PUYAN MOJABI (Member, IEEE)

Department of Electrical and Computer Engineering, University of Manitoba, Winnipeg, MB R3T 5V6, Canada

CORRESPONDING AUTHOR: C. NIU (e-mail: niuc@myumanitoba.ca)

ABSTRACT A deep learning approach based on a diffusion model is proposed to yield metasurface unit cell designs. This method takes desired two-port scattering parameters along with the frequency of operation in an attempt to synthesize three-layered metasurface unit cells. The core of this approach lies in casting the three-layered unit cell synthesis process as conditional three-channel binary image synthesis. The conditions are governed by the desired scattering parameters at a given frequency whereas the binary nature implies the presence and absence of metallic traces. Once synthesized, these unit cells are placed beside each other, without any further tuning, to form the final metasurface. The performance of the whole metasurface, for three different design scenarios, is then tested against full-wave simulation and/or experimental data.

INDEX TERMS Deep learning, diffusion models, metasurfaces, unit cells, radiation pattern synthesis.

I. INTRODUCTION

ELECTROMAGNETIC (EM) metasurfaces are thin artificial materials that can tailor incoming EM waves into desired outgoing EM waves [1]. This tailoring is achieved through the interaction of the incoming EM waves with the subwavelength constituents of the metasurface known as unit cells. The metasurface design procedure can be divided into macroscopic and microscopic steps [2]. In the macroscopic step, the required tangential EM fields on the faces of the metasurface are obtained and then used in conjunction with the generalized sheet transition conditions (GSTCs) [3] to calculate the required surface properties of the metasurface (e.g., surface susceptibilities). This step typically begins by the designer specifying some desired performance criteria such as main beam directions, null angles, and sidelobe levels to be realized by the EM wave transformation performed by the metasurface. These performance criteria will then used to infer the required tangential fields on the faces of the metasurface using various techniques such as solving an inverse problem [4], [5], [6], [7], antenna array techniques [8], or machine learning approaches [9]. The macroscopic step can be made to be fully automated, which provides a significant advantage for radiation pattern synthesis using metasurfaces.

On the other hand, the microscopic step deals with the physical design of unit cells so as to realize the required surface properties obtained in the macroscopic step. At microwave and mm-wave frequencies, this is mostly achieved by patterned metallic claddings supported by dielectric substrates [11], [12], [13]. To this end, look up tables are often formed through running a large number of full-wave unit cell simulations, which record the scattering response of subwavelength scatterers (e.g., copper dogbone shaped inclusions [14]) of varying dimensions. However, lookup tables are typically formed for single-layer metallic scatterers, and thus do not take into account the near-field coupling in multi-layered metasurface design scenarios. We note that multi-layered designs (e.g., employing three-layer [12] or four-layer [15] unit cells) are important as they provide more degrees of freedom to enable functionalities such as reflectionless wide-angle refraction [16]. To handle this issue, methods such as [17] are proposed to incorporate the near-field coupling effect in the unit cell design procedure. In particular, the method presented in [17] augments
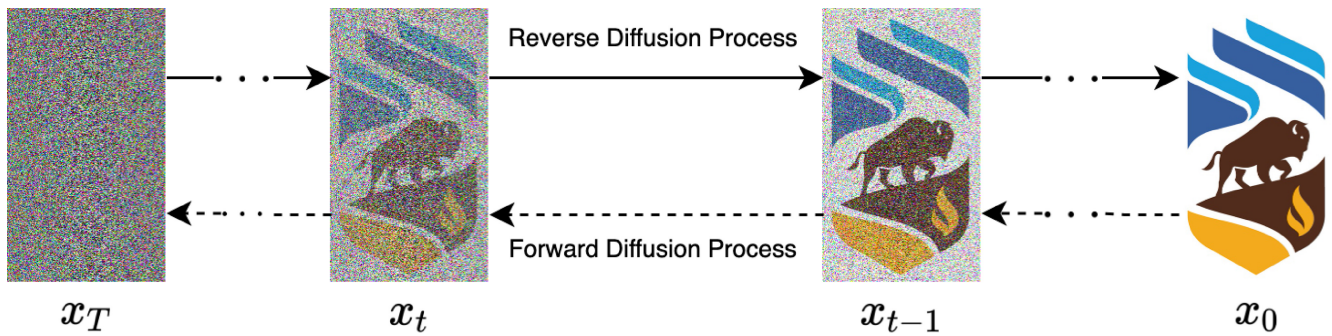
FIGURE 1. An illustration of the diffusion process for diffusion models. The dashed and solid arrows represent the forward and reverse diffusion processes, respectively. This is based on [10].

the basic unit cell circuit model [11] by current-controlled voltage sources in an attempt to take into account mutual coupling. Although these techniques have shown promising results, they may require further optimization and fine tuning in a full-wave forward solver, which can be time consuming. Thus, as opposed to the macroscopic design, the microscopic design step is not yet fully automated. Therefore, it is useful to provide the microscopic design step with an appropriate initial guess, which is the focus of this paper.

To provide an appropriate initial guess for the microscopic design, we employ a deep learning approach. Deep learning has emerged as the state-of-the-art solution for numerous challenges in the computer science domain, including computer vision [18], natural language processing [19], and generative tasks such as text-to-image synthesis [20]. The application of deep learning techniques, particularly generative modeling, to metasurface design may effectively enable the end-to-end metasurface design process, i.e., beginning the design from desired performance criteria and arriving at the required patterned metallic claddings. In fact, generative deep learning techniques have been already utilized in the synthesis of single- and multi-layered metasurfaces at both microwave [21], [22], [23], [24], [25], and visible/near infrared spectra [26], [27]. The existing generative deep learning techniques for metasurface design mainly consist of generative adversarial networks (GAN) [28], [29], [30], variational auto-encoders (VAE) [31], [32], [33], and combinations of deep learning techniques with conventional optimization techniques [34], [35].

Herein, we employ a deep learning approach based on diffusion models [36] for multi-layered unit cell designs. To the best of the authors' knowledge, this is the first time that diffusion models have been used for this purpose. Currently, diffusion models are state-of-the-art techniques for image synthesis applications. Casting multi-layered unit cells as multi-channel images, we investigate the performance of diffusion models to generate unit cells from desired scattering parameters. (Note that the desired scattering parameters can be easily calculated from the required surface properties of the metasurface [37, Ch. 4], which are obtained in the macroscopic design step.) The main advantage for

using diffusion models as compared to GANs is to avoid training instabilities [10]. In addition, diffusion models offer more model complexities compared to the VAE, thus, having the potential for better performance. The performance of the proposed deep learning approach is evaluated using both full-wave simulations and experimental data. To this end, we designed three metasurfaces under three different design scenarios by utilizing the unit cells obtained directly from the proposed deep learning approach; i.e., no further optimization has been applied to these unit cells. Thus, the deep learning method presented in this paper can be viewed as a means to generate initial guess designs, which can be further tuned using full-wave solvers. In what follows, we implicitly assume a time dependency of $\exp(j\omega t)$ where ω and t denote the angular frequency and time respectively. Finally, we note that this paper is the extension of our conference paper [38].

II. SCOPE AND PROBLEM STATEMENT

Herein, we focus on the design of omega-bianisotropic transmitting Huygens' metasurfaces [39]. These metasurfaces can be implemented by employing three-layered unit cells. The unit cells considered herein employ dogbone shaped metallic traces [12], [14] in the X-band frequency range (8.2 GHz to 12.4 GHz). These metasurfaces can offer electric-to-electric, magnetic-to-magnetic, and magnetoelectric surface susceptibilities [12], thus enabling important functionalities such as wide-angle perfect refraction [16]. We further limit ourselves to lossless and passive unit cells, except for the inevitable loss of the dielectric substrate and the fabricated copper traces. It should be noted that the above scope is merely used to limit the computational complexity associated with the data generation process for neural network training purposes. The proposed deep learning approach can therefore be extended to go beyond this scope.

The objective of this paper can be described as follows. Given a desired EM wave transformation and an EM incident field, we obtain the required two-port scattering parameters for each metasurface unit cell. These scattering parameters along with the frequency of operation is fed to the proposed deep learning diffusion model, which then yields dogbone-shaped three-layered unit cell designs. These unit

cell designs are then combined to form the whole metasurface so as to evaluate its performance against the desired transformation. These metasurfaces have spatial modulations in one direction along the metasurface plane and are fully periodic in the other direction; thus, they will be evaluated under two-dimensional (2D) transverse magnetic (TM) or transverse electric (TE) wave propagation.

III. BACKGROUND AND METHODOLOGY

The deep learning models developed in this work are largely inspired by the conditional image synthesis in the field of computer science. In particular, we have modified the latent diffusion model (LDM) [40] to be able to synthesize metasurface unit cells. The structure of these unit cells includes three-layered patterned metallic claddings supported by thin dielectric substrates. These metallic claddings are modelled as perfect electric conductors (PEC) in the data generation process, and thus are referred to as PEC traces in this paper. These three-layered PEC traces are to be designed from the knowledge of required scattering parameters. Since the unit cells are treated as two-port networks, the desired scattering parameters will be a 2×2 complex matrix. In the context of conditional image synthesis, these scattering parameters (along with the frequency of operation) can be viewed as the conditions for synthesizing images, which are the unit cell's PEC traces. The LDM belongs to a family of generative techniques called diffusion models [10], [36], [41]. In this section, we discuss the background and implementation of the diffusion models and in particular LDM.

A. DIFFUSION MODELS (DM)

Diffusion models are a type of generative models that are inspired by non-equilibrium thermodynamics [41]: molecules diffuse from high-density to low-density areas due to entropy. This can be viewed as losing the information associated with their initial state. This is conceptually similar to an aspect of information theory where information within the data can be lost due to gradual intervention of noise. The key concept behind diffusion models is to build a machine learning system that is capable of recovering the information back from noise by learning the systematic information decay. Diffusion models consist of forward and reverse processes. The forward diffusion process defines a Markov chain of diffusion steps to slowly add random noise to data. More importantly, the reverse diffusion process aims to learn to gradually remove noise so as to yield the data of interest. In the forward diffusion process, given the data x_0 and a noising mechanism, we progressively generate the intermediate noisy data, say from x_1 to x_T, through a recursive process [41]. The generative capability of the diffusion models comes from the reverse diffusion process that attempts to recreate the original data x_0 from x_T. Therefore, the goal of the diffusion models is to train a neural network that is able to "denoise" back in time, i.e., from x_T to x_0. The forward and reverse processes of the diffusion models are shown in Fig. 1.
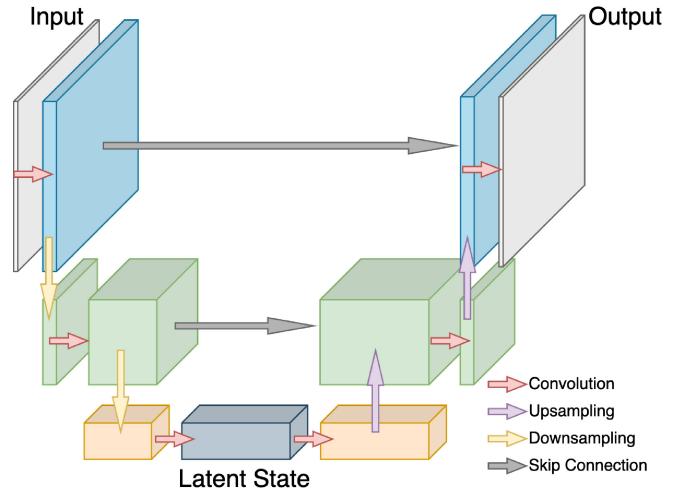

FIGURE 2. An illustration of the U-Net architecture. This is based on a similar figure in [42].
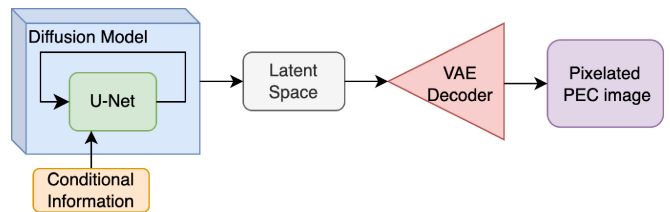

FIGURE 3. An illustration of the latent diffusion model (LDM). The conditional information, in our case, is the desired two-port scattering parameters along with the frequency of operation.

In general, the diffusion model is designed to generate random data from noise, e.g., generating random human faces. However, this is not useful for our unit cell design application since the generation of PEC traces needs to be associated with the desired two-port scattering parameters. To this end, with minor modifications, diffusion models are able to synthesize data samples based on conditional information such as class labels (e.g., white male human face) or in our case based on the desired scattering parameters and the frequency of operation. This is achieved by injecting this additional information within each reverse diffusion step. The reverse diffusion process can be implemented by different neural networks. Herein, we utilize the U-Net [42] as the neural network of choice.

B. U-NET

U-Net [42] was originally designed for image segmentation tasks for medical imaging where the goal is to classify each pixel of the input image to produce a segmentation map. A basic structure of the U-Net is shown in Fig. 2. The U-Net distills the input image to a latent state through a series of downsampling steps and constructs the segmentation map (the output) through a series of upsampling steps. The key innovation behind the U-Net is the skip connections that link each stage of downsampling to its upsampling counterpart. These skip connections allow the gradients to have the
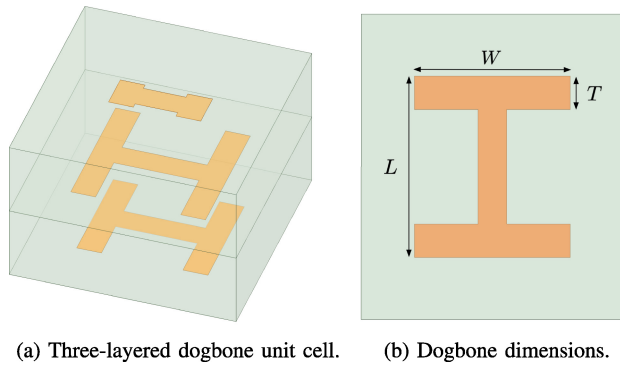
(a) Three-layered dogbone unit cell. (b) Dogbone dimensions.

FIGURE 4. The parameters *L*, *W*, and *T* are the length, width and trace width of the dogbone. As shown in the left figure, these three dogbone layers are supported by two dielectric substrates (Rogers RO3010).

FIGURE 5. The three-channel pixelated binary image of dogbones (not to scale).

chance to flow directly from upsampling stages to the corresponding downsampling ones. This reduces the effect of vanishing gradients [42], thus, improving the performance of the neural network. In a typical implementation of the U-Net, the sizes of the input and output data are identical. This feature is suitable for diffusion models as the sizes of x_0 to x_T remain the same.

C. LATENT DIFFUSION MODEL (LDM)

Although diffusion models have achieved the state-of-the-art performance in many image synthesis tasks [10], the original implementation of diffusion models often suffers from computational cost in order to achieve high-quality generation. The latent diffusion model (LDM) was developed to address this issue by compressing the raw input image before the diffusion process [40]. This separates the overall image synthesis into two steps: compression and generation. For the compression stage, a variational autoencoder (VAE) [31] is utilized while a diffusion model (in our case, the U-Net) is used for the generation stage. As a result, the raw input image is first compressed into a latent space by VAE. In the generation step, the diffusion model only operates (i.e., denoises) in the latent space, hence the name latent diffusion model. By operating in the compressed latent space as opposed to the raw image space, the LDM offers improved memory efficiency and significantly reduces the overall computational complexity.

IV. UNIT CELL DESIGN

A neural network model based on the LDM was developed in order to synthesize unit cells from desired two-port scattering parameters at a given frequency of operation. We consider three-layered unit cells where the PEC traces are in the shape of dogbones as shown in Fig. 4. The size of each unit cell is one-sixth of the wavelength at 12.4 GHz, which is about 4 mm × 4 mm. These PEC dogbones are supported by two dielectric substrates which are assumed to be Rogers RO3010 substrates with the relative permittivity of 10.2,
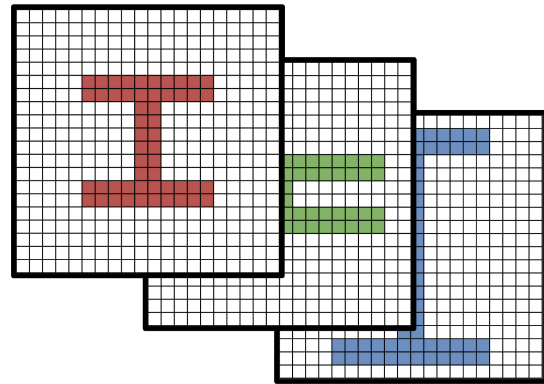
thickness of 1.28 mm, and the loss tangent of 0.0035.[1] There are three parameters that govern the shape of each dogbone: width, length, and trace width. In our implementation, similar to [14], we have fixed the trace width[2] while varying width and length values to generate different surface properties. Thus, a given three-layered unit cell can be represented by six different W and L (i.e., two per layer).

The input to this network, in our implementation, is a real-valued vector of length seven ($\mathbb{R}^{7 \times 1}$) that consists of the operating frequency as well as the real and imaginary parts of the following scattering parameters: S_{11}, S_{12}, and S_{22}. (Since our unit cells are reciprocal, $S_{12} = S_{21}$.) We refer to this $\mathbb{R}^{7 \times 1}$ vector as the input vector. Given this input vector, the generated output of the neural network is a three-channel binary image of the pixelated three-layered dogbone unit cell design, see Fig. 5. The presence and absence of PEC pixels represents the binary aspect of this image. In our implementation, this will be a $3 \times 128 \times 128$ tensor, which means 128×128 pixels per layer. (The number of pixels should be chosen based on the possible fabrication precision.) We refer to this tensor as *pixelated PEC image*. Finally, we note that for our design parameters, there exist 7.62×10^{11} possible designs.[3]

As noted earlier, we utilize the LDM to generate unit cells from given input scattering parameters. The LDM consists of two main components that need to be trained separately. Firstly, the VAE is trained to encode pixelated PEC images to a latent space and vice versa for the decoding. Secondly, the diffusion model, implemented in the U-Net, is trained to synthesize latent tensors based on desired input vectors. In

---

1. For fabrication purposes, see Section V-A, these two Rogers RO3010 substrates are bonded by a 1.5 mil (≈ 0.04 mm) Rogers 2929 bondply. Due to the small thickness of this bondply, its presence has been ignored in the unit cell synthesis process.

2. In our design, we have fixed the trace width to $T = 0.441$mm, which is equivalent to 14 pixels in the pixelated PEC image.

3. Each dogbone is generated on a 128×128 canvas with a trace width fixed at 14 pixels. Thus, the width and length of the dogbone varies from 20 to 124 and from 38 to 124 pixels respectively. Consequently, for one layer there are $(124 - 20 + 1) \times (124 - 38 + 1) = 9135$ possible designs. With three layers there will be $9135^3 = 7.62 \times 10^{11}$ designs.

the following two subsections, these two training procedures are described.

A. VAE DATASET GENERATION AND TRAINING

We employ a standard VAE that is constructed using a convolutional neural network to distill pixelated PEC images into latent tensors for the training and prediction of the LDM. Since the VAE is an unsupervised network (i.e., it only requires pixelated PEC images without their corresponding scattering parameters), we do not need to perform full-wave simulations in its training process. To fully take advantage of this feature such that the VAE network can explore the problem space as much as possible, pixelated PEC images are randomly generated. In fact, in order to speed up the training process and avoid wasting hard-drive space, random pixelated PEC images are generated "on-the-fly" in parallel with the training process. The resulting latent tensor has the size of $4 \times 8 \times 8$, which can be compared to a pixelated PEC image having the dimension of $3 \times 128 \times 128$.

B. DM DATASET GENERATION AND TRAINING

The DM that was developed in this work closely follows the original network developed in [40]. The backbone of this diffusion network is the U-Net with convolutional layers. To synthesize unit cells based on desired scattering parameters and the frequency of operation, the input vector is injected into each layer of the U-Net through a cross-attention mechanism. It should be noted that the original LDM implementation introduced domain-specific encoders to handle various types of conditional information (e.g., generating images from class labels or text prompts). However, since our network is specific to unit cell synthesis from a single set of particular conditional information (i.e., scattering parameters and the frequency of operation), we omitted the implementation of domain-specific encoders.

To generate a large and diverse dataset for the training of the DM, we have developed an automated dataset generator to produce a labeled dataset. This dataset generator uses Ansys HFSS as its full-wave simulation engine. Each unit cell was simulated under periodic boundary conditions excited by Floquet ports.[4] The size of the training dataset is about $500,000$ and the testing dataset has a size of about $50,000$ which was hidden during the training process. A primary challenge encountered during the training process of the developed DM pertains to its premature overfitting. That is, at the early stage of training, we observed a rising loss in the testing dataset while the training dataset loss continued to decrease. This is likely associated with our small dataset size compared to the vast possibilities for unit cell designs (7.62×10^{11} possible designs as noted in Section IV). To handle this issue, we developed a neural

network model based on EfficientNet [45], which predicts the two-port scattering parameters for given pixelated PEC images. This forward solver was trained by the aforementioned Ansys HFSS dataset. Once trained, it was applied to randomly generated PEC images so as to augment the original Ansys HFSS dataset. In particular, the labeled datasets generated by Ansys HFSS and our forward solver contribute to 95% and 5% of the overall labeled dataset respectively. This enriched dataset was then used to train the DM where the 5% synthetic data was refreshed at each epoch. This approach successfully mitigated the overfitting issue, thereby enhancing the overall performance of the DM.

During the generation process, for a given metasurface design, a list of desired two-port scattering parameters associated with each metasurface unit cell and the operational frequency is fed to the developed LDM. For given two-port scattering parameters, the neural network will on average generate ten unique pixelated PEC images. To minimize the simulation setup in Ansys HFSS, an image processing technique is applied to these uniquely generated pixelated PEC images to find its corresponding dogbone design parameters (width and length for each layer), which can then be easily modeled in Ansys HFSS. These unique dogbone unit cell designs along with their achieved two-port scattering parameters are then recorded to a dataset for the final metasurface design. When constructing the entire metasurface, for each unit cell, we will find the dogbone design whose achieved scattering parameters are "closest" to the desired values. It should be noted that we can employ a few different strategies to find the "closest" dogbone designs. For example, we can optimize for both S_{11} and S_{21} with an equal weight, optimize for S_{11} individually, or merely S_{21} by minimizing the following cost functions

$$\mathcal{C}_1 \triangleq 0.5\Big(|S_{11}^{\text{desired}} - S_{11}^{\text{achieved}}| + |S_{21}^{\text{desired}} - S_{21}^{\text{achieved}}|\Big), \quad (1)$$

$$\mathcal{C}_2 \triangleq \Big(|S_{11}^{\text{desired}} - S_{11}^{\text{achieved}}|\Big), \quad (2)$$

$$\mathcal{C}_3 \triangleq \Big(|S_{21}^{\text{desired}} - S_{21}^{\text{achieved}}|\Big), \quad (3)$$

respectively. Finally, we note that the generation time for the LDM to create unit cell designs (on average, 10 unit cell designs for a given set of scattering parameters) is approximately 7 seconds with the neural network running on an Nvidia Tesla V100. In addition, the HFSS simulation time to evaluate these dogbone unit cells typically ranges from 1 to 8 minutes per unit cell. Thus, the main computational cost of this generation approach is associated with the HFSS run time to single out one unit cell design for a given set of scattering parameters.

V. RESULTS

In order to evaluate the performance of the developed neural network for the synthesis of electromagnetic metasurface unit cells, we consider three design examples. In each example, we first briefly talk about the procedure we used to obtain the required two-port scattering parameters for each unit cell
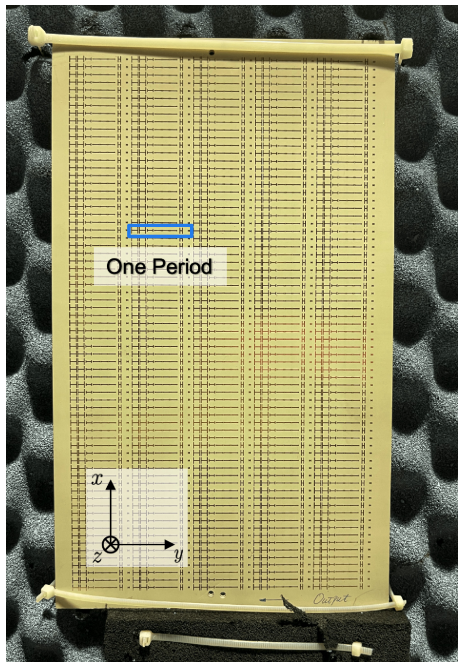
---

4. Due to the use of periodic boundary conditions to characterize the two-port scattering parameters of unit cells, the final metasurface design is still under the local periodicity approximation [43], which can degrade the performance of aperiodic metasurfaces considered herein. Recently, techniques such as [44] have been proposed to tackle this approximation.

FIGURE 6. The fabricated metasurface (for the wide-angle refraction example). The output face of the metasurface is visible in this figure. The spatial modulation is along the *y* axis, with no variation along the *x* axis. Five periods have been used along the *y* axis, with eight unit cells in one period.

(i.e., the macroscopic design step). We then pass these scattering parameters to the LDM to design the unit cells. The performance of the LDM is then reported based on the cost functionals in (1)-(3) as well as the quality of the required wave transformation achieved by the whole metasurface. The dimensions of the unit cells for each design example can be found in the Appendix. We emphasize that no further optimizations have been applied on these unit cells and that they are taken directly from the LDM.

A. PLANE WAVE REFRACTION

For the first example, we design and evaluate a refracting metasurface operating under the 2D TM case. As shown in Fig. 6, the metasurface lies in the *xy* plane, centered at the origin, with the spatial modulation along the *y* axis. The metasurface has no variation along the *x* axis, hence the 2D assumption. Noting that the design is under the 2D TM assumption with the propagation plane being the *yz* plane, the EM field components will be H_x, E_y, and E_z. It has been shown in [46] that Snell's law at the interface of two dielectric media can be generalized when a phase profile is engineered along the interface. A properly designed metasurface when placed at the interface can support the required phase profile. Assuming free space on both sides of the metasurface, refracting a plane wave incident at the angle θ_i (with respect to the normal vector) on the metasurface to the angle θ_t requires a periodic metasurface with the periodicity of

$$P = \frac{\lambda_0}{\sin \theta_t - \sin \theta_i}, \qquad (4)$$

where λ_0 is the wavelength of operation in free space [46]. In our case, the incident plane wave impinges normally on the metasurface ($\theta_i = 0$); thus, $P = \lambda_0/\sin \theta_t$. Assuming the desired refraction angle to be 69.6° and the frequency of operation to be 10 GHz, the periodicity will be about 32 mm. Noting that the size of each unit cell is about 4 mm, this requires eight unit cells per period. To enable perfect refraction, the scattering parameters associated with each unit cell need to be properly designed to satisfy the local power conservation (LPC) constraint [13], which can also be justified using the generalized scattering parameters [16]. It has been shown in [12], [16], [47], [48] that perfect refraction can be achieved by omega bianisotropic metasurfaces. The unit cells considered herein can provide omega bianisotropy due to the possibility of having an asymmetric structure (i.e., the top and bottom dogbones being different) [13], and can thus be used for this purpose.

To begin the design process, we first assume that the tangential fields on the input face of the metasurface due to a normally incident plane wave (travelling in the $-\hat{z}$ direction) are

$$E_y^{\text{input}} = E_i, \qquad H_x^{\text{input}} = E_i/\eta_0 \qquad (5)$$

where η_0 is the intrinsic impedance of free space and E_i is the amplitude of the incident plane wave. (Due to the assumption of a reflectionless metasurface, the input tangential fields will only be affected by the incident field.) Assuming that the output wave is plane wave refracted by θ_t, the tangential fields on the output face of the metasurface will be

$$E_y^{\text{output}} = E_t \cos \theta_t e^{-jk_0 y \sin \theta_t} \qquad (6)$$

$$H_x^{\text{output}} = \frac{E_t}{\eta_0} e^{-jk_0 y \sin \theta_t} \qquad (7)$$

where E_t is the amplitude of the refracted plane wave. As noted in [47], [49], if E_t is chosen as

$$E_t = \frac{|E_i|}{\sqrt{\cos \theta_t}} e^{j\varphi}, \qquad (8)$$

where φ is an arbitrary constant phase, the LPC constraint is met and perfect refraction using a lossless and passive metasurface can be obtained. Now that we know the input and output tangential fields, we discretize *y* in (6) and (7) into eight equally spaced unit cells so as to cover the whole period *P*. Knowing the properties of the Rogers RO3010 substrate, we can obtain the required impedance values for each unit cell similar to the procedure explained in [48]. These unit cell properties can then be easily represented by two-port ABCD parameters. The ABCD representations are then converted to the two-port scattering parameter representation [50].[5] These two-port scattering parameters are then fed to the LDM to yield dogbone-based unit cell designs.

As noted earlier, the LDM outputs a few designs for a given two-port scattering matrix. We then need to single out

---

5. For further verification, each of these two-port scattering matrices is converted to the two-port generalized scattering matrix [16] to make sure that the absolute of the generalized forward scattering parameters is unity.
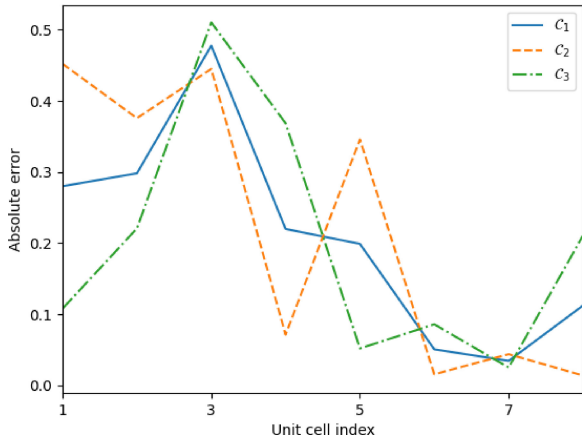
FIGURE 7. The absolute error of the achieved scattering parameters for each unit cell with respect to the desired ones for the plane wave refraction example. Each period consists of eight unit cells. The final unit cell design is based on C_1. The values of C_2 and C_3 are also reported for the sake of completeness.
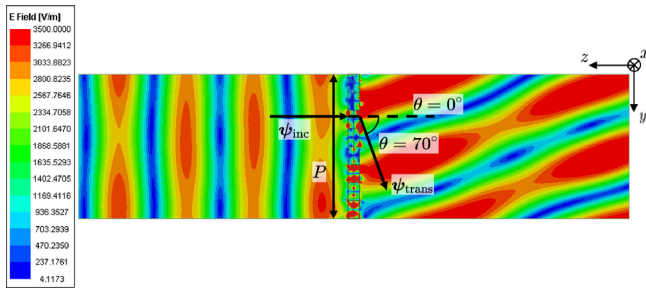

FIGURE 8. Plot of the electric field magnitude at a fixed phase in Ansys HFSS. In this simulation, one period (P) of the metasurface has been used and the metasurface is enclosed by the periodic boundary conditions. In addition, PEC baffles have been used for this simulation. The left side of the metasurface is its input side (illuminated by ψ_{inc} where ψ denotes $\{E, H\}$) and the right side of the metasurface is its output side yielding the refracted wave ψ_{trans}.

FIGURE 9. Plot of the electric field magnitude at a fixed phase for the truncated metasurface where five periods ($5P$) are used to form the truncated metasurface (comprising of 40 unit cells and no PEC baffles). From each side, the metasurface is extended by quarter-wavelength absorbers.

FIGURE 10. The normalized far-field power pattern plots of the truncated metasurface ($5P$ aperture size) for three cases: (i) Ansys HFSS simulation of the metasurface consisting of dogbone-shaped unit cells, (ii) Ansys HFSS simulation of the metasurface consisting of ideal impedance sheet unit cells, and (iii) the measured far-field power pattern of the fabricated metasurface. (The "correction factor" of $\cos\theta$ has not been applied to any of these plots.)

one design from these multiple potential solutions. To this end, for each unit cell, each of the potential solutions is evaluated by calculating C_1 in (1), with the chosen dogbone unit cell being the one that minimizes C_1. (For the dimensions of these unit cells, see the Appendix.) The achieved scattering parameters of these dogbones are compared to the desired scattering parameters in Fig. 7 by plotting C_1 for each unit cell. Although not used for this example, the values of C_2 and C_3 have also been reported in the same figure. Noting C_1, it can be seen that the performance of the first three unit cells is worse than the remaining unit cells. This is partly due to the fact the phase of the desired S_{21} for the first unit cell is close to zero degrees. As noted in [51], this unit cell will then be close to resonance, and meeting its desired scattering parameters can be quite challenging. The presence of the resonance for this unit cell was further indicated by the lossy behaviour of this unit cell as also observed in [51]. These unit cells are then used to form the metasurface. The near-field simulation of this metasurface under the periodic boundary condition and perfect electric conductor baffles [14] is shown in Fig. 8, which shows small reflections on the input (left) side and also a refracted plane
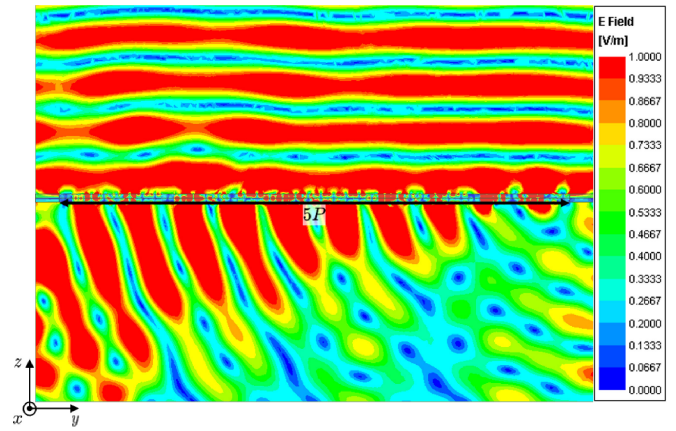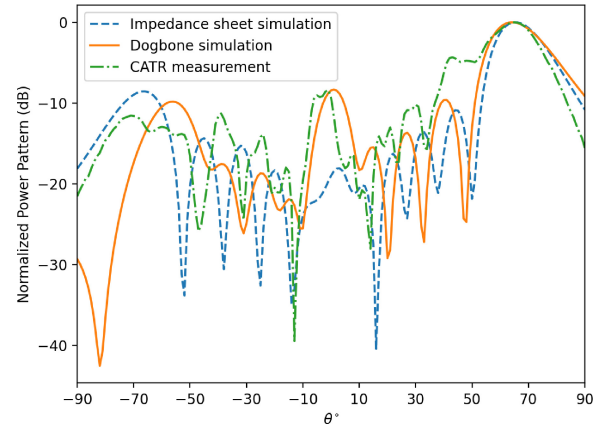
wave in the output (right) side. The achieved refraction angle, measured geometrically, is about 70° which is very close to the desired refraction angle. In addition, according to the Floquet mode analysis by Ansys HFSS, the *refraction power efficiency* (power contained within the desired Floquet mode with respect to the total power) of this metasurface is about 75%.

For manufacturing purposes, we now limit ourselves to only five periods of this metasurface and also remove the baffles for the ease of fabrication. The near-field simulation of this *truncated* metasurface is shown in Fig. 9. The far-field power pattern obtained from this metasurface is shown in Fig. 10 (orange). The angle of the main beam is at 64°. The reason that this achieved main beam angle is not closer to the desired refraction angle of 69.6° can be justified by noting that the design process assumes a fully periodic boundary condition which effectively means that the metasurface aperture is of infinite length. In addition,
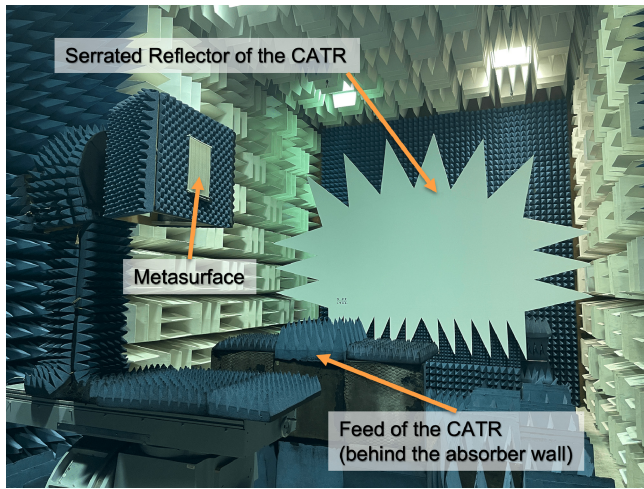
FIGURE 11. The far-field measurements of the fabricated metasurface in a compact antenna test range (CATR). The output face of the metasurface, i.e., the face that is supposed to interact with a plane wave at 69.6°, is illuminated by the serrated reflector.
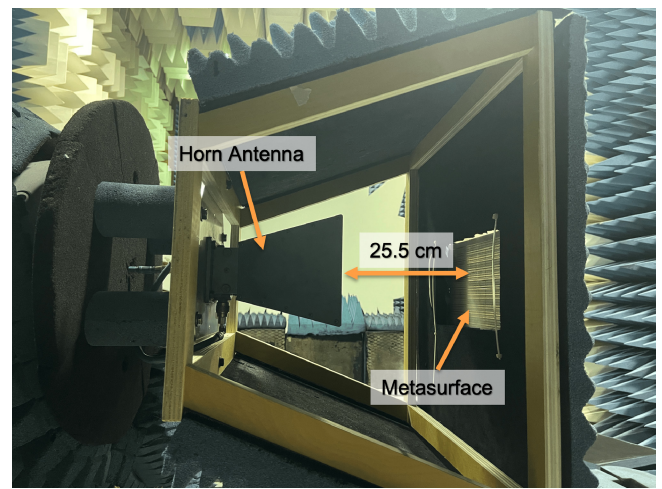

FIGURE 12. The metasurface mounting and the receiving horn antenna. The horn antenna is located on the input side of the metasurface (i.e., the side that is supposed to interact with a normally incident plane wave).

this fully periodic assumption means that the effective aperture size of the metasurface remains the same from any angles. However, this is not the case for the truncated metasurface, which has an aperture size of five periods. This finite aperture size results in a reduced effective aperture size (by a factor of $\cos\theta$) when radiating at $\theta \neq 0$. As noted in [48], this discrepancy between a fully periodic aperture and a truncated one can be numerically compensated to yield the expected refraction angle, i.e., the main beam angle that would have been obtained if the metasurface had many more periods. Applying this correction factor to the whole pattern, the expected refraction angle becomes 68°, which is closer to the desired 69.6°. To compare this with a more ideal situation, Fig. 10 (blue) shows the far-field power pattern of this metasurface when the unit cells are modeled using impedance boundary conditions instead of dogbones. As can be seen, this ideal power pattern exhibits a lower side lobe level around $\theta = 0$ with a main beam angle at 65°. Applying the above correction factor to the whole pattern, the expected refraction angle becomes 68°.

We have also fabricated this metasurface as shown in Fig. 6. As can be seen, along the y axis, we have used five periods, and along the x axis, we have repeated the dogbones 70 times to mimic a 2D condition (i.e., $\partial/\partial x = 0$). This fabricated metasurface has then been tested in a compact antenna test range (CATR) as shown in Fig. 11. Once the feed of the CATR illuminates the serrated reflector, a plane wave condition is created in the quiet zone of the CATR. The metasurface under test is then placed in this quiet zone such that its output face is looking toward the reflector. On the input side of the metasurface, a horn antenna is placed to receive the electromagnetic wave passing through the metasurface. This horn antenna is shown in Fig. 12 where the distance between the input face of the metasurface and the horn aperture is 25.5 cm (equivalent to about $8.5\lambda_0$). The horn-metasurface structure is then rotated from $-90°$ to $+90°$
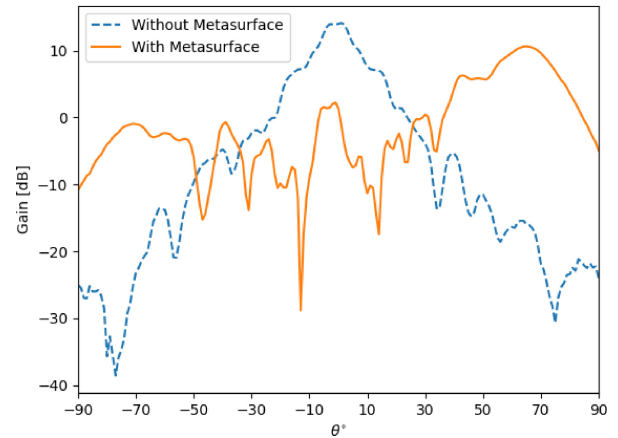

FIGURE 13. The gain pattern obtained from the CATR measurements with and without the metasurface. The maximum gain of the horn antenna structure with and without the metasurface are 14.1 dB and 10.6 dB respectively.

with respect to the boresight of the serrated reflector. The recorded power pattern of the horn-metasurface structure at the frequency of operation (10 GHz) is then shown in Fig. 10 (green). The main beam angle is at 65°. After applying the correction factor, the expected refraction angle will be at 67°.

Finally, the transmission power efficiency of the truncated metasurface, shown in Fig. 9 and obtained from HFSS simulation, is 71.07%. (This efficiency is defined as the ratio between the normal real power leaving the metasurface and the normal real power incident to the metasurface.) We have not obtained the transmission power efficiency from measurements. However, we have compared the maximum gain of the horn-metasurface structure with the gain obtained when the metasurface is removed (while the absorbing structure remains around the horn) as shown in Fig. 13. As can be seen, the maximum gain has dropped from 14.1 dB to
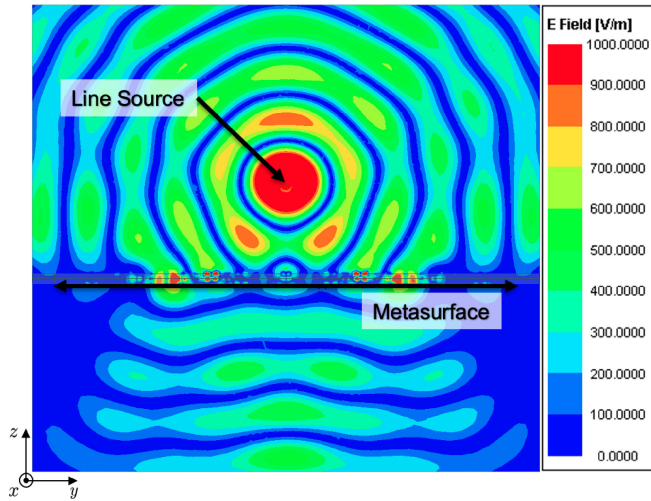
FIGURE 14. Plot of the electric field magnitude at a fixed phase. The metasurface is illuminated by a line source and then transforms the incident cylindrical wave to a truncated plane wave.
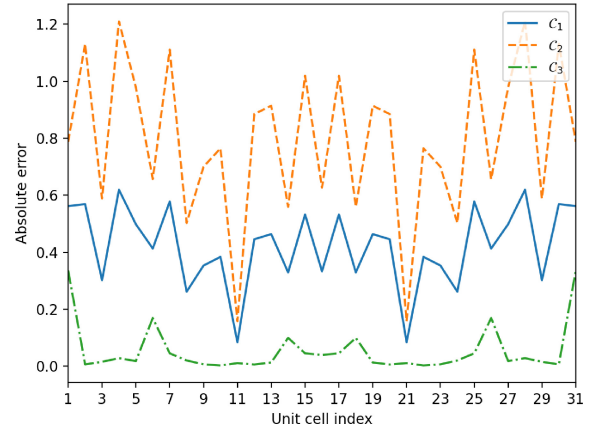

FIGURE 15. The absolute error of the achieved scattering parameters for each unit cell with respect to the desired ones for the circular wave to plane wave transformation example. The metasurface consists of 31 unit cells. The final unit cell design is based on $\mathcal{C}_3$. The values of $\mathcal{C}_1$ and $\mathcal{C}_2$ are also reported for the sake of completeness.

10.6 dB when the metasurface is added to the horn-absorbing structure.

B. CYLINDRICAL WAVE TO PLANE WAVE TRANSFORMATION

This design example aims to transform the cylindrical wave generated by a line source into a plane wave; see Fig. 14. The distance from the line source to the input face of the metasurface is one wavelength at the operational frequency of 12.4 GHz. This example is under the 2D TE assumption; thus, since the plane of propagation is the yz plane, we have three field components: E_x, H_y, and H_z. The metasurface consists of 31 unit cells and has an aperture size of about $5.2\lambda_0$. Due to the difference between the power profiles associated with the line source and plane wave in the input and output faces of the metasurface, LPC is not satisfied. To meet the LPC constraint, auxiliary surface waves [7], [15], [52], [53] are employed according to the procedure explained in [53]. In this approach, an auxiliary surface wave is added to the input face of the metasurface that redistributes the power between the unit cells while being evanescent (exponentially decaying) in the direction normal to the metasurface; thus, no real power is reflected (or lost) in the ideal scenario. After augmenting the input tangential fields (resulting from the line source) with the fields due to this auxiliary surface wave, the desired two-port scattering parameters are obtained similar to the procedure explained for the plane wave refraction example. These two-port scattering matrices are then fed to the LDM.

As noted earlier, the LDM yields a few potential unit-cell solutions per given two-port scattering parameters. To single out a unit cell, we evaluate $\mathcal{C}_3$ in (3) for these potential solutions, and choose the one that corresponds to the minimum value. The values of $\mathcal{C}_3$ for the chosen unit cells are plotted in Fig. 15. Although we have not used $\mathcal{C}_1$ and $\mathcal{C}_2$ to choose the final unit cells, their values have been plotted for the

final unit cells. Since the unit cells are chosen based on $\mathcal{C}_3$ (focused on S_{21} performance), the error associated with S_{21} is good, but the other two errors are large. These unit cells are then simulated in Ansys HFSS as shown in Fig. 14. Although the resulting plane wave is not of high quality, we do see fields with planes of constant phase emanating from the metasurface, and a certain uniformity in the magnitude. The power transmission efficiency of this metasurface is 66.85%. Similar designs using conventional techniques (i.e., lookup tables followed by further iterative dimension tuning) have shown slightly better performance as compared to this example, e.g., see [54]. However, the main advantage of our design is that it has not gone under any further optimizations. Thus, it can be used as an initial guess for further tuning.

C. FROM FAR-FIELD PERFORMANCE CRITERIA TO METASURFACE DESIGN

For the last example, we consider an end-to-end design procedure where the designer identifies the following: (i) desired far-field performance criteria to be achieved, (ii) the line source excitation and its distance from the metasurface ($1\lambda_0$), (iii) the aperture size of the metasurface ($6.5\lambda_0$) along with the frequency of operation (12.4 GHz) employing 39 unit cells. Similar to the previous example, this design is pursued under the 2D TE assumption. The desired far-field performance criteria are shown in Fig. 16 where "•" shows the desired two main beam angles, "×" denotes the desired null angles, and "—" represents the half-power beamwidths (HPBWs). Finally, the two horizontal lines in Fig. 16 show the desired sidelobe levels (SLLs) and maximum null levels.

To find the required two-port scattering parameters for each unit cell, we need to know the required tangential fields on the metasurface aperture. To this end, we can employ inversion methods such as [4], [5], [6], [9] to infer these tangential fields from the knowledge of desired far-field performance criteria. Herein, the procedure developed in [9]
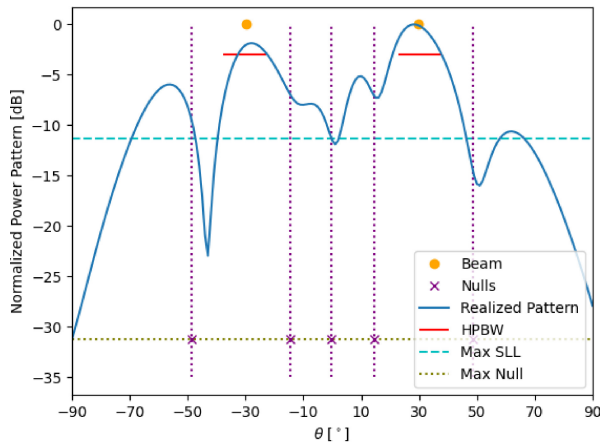
FIGURE 16. The achieved far-field power pattern from the metasurface designed to meet the desired far-field performance criteria.
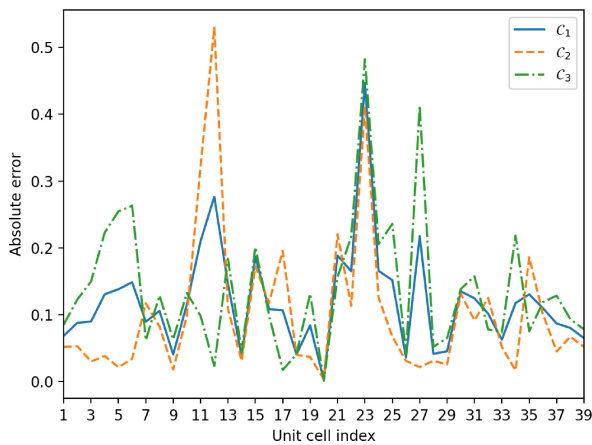

FIGURE 17. The absolute error of the achieved scattering parameters for each unit cell with respect to the desired ones for the performance criteria design example. The metasurface consists of 39 unit cells. The final unit cell design is based on C_3. The values of C_1 and C_2 are also reported for the sake of completeness.

was used to find these tangential fields and subsequently the required unit cells' two-port scattering matrices. Once the required two-port scattering matrices are found, they are fed to the LDM. The potential solutions for each unit cells are singled out by evaluating C_3 in (3). The values of C_3 for the metasurface's 39 unit cells are shown in Fig. 17. Similar to the previous example, the values of C_1 and C_2, although not used in this design process, are reported in this figure for the sake of completeness. The obtained unit cells are then placed together to form the final metasurface.

As shown in Fig. 18, the metasurface is simulated in Ansys HFSS, which shows the presence of the two beams on its output side. In addition, the cylindrical incident wave on the input side is somewhat distorted, which shows the presence of undesired reflections on the input side of the metasurface. The resulting far-field power pattern is obtained and shown in Fig. 16 (solid blue curve). For this example, the realized main beam angles are close to the desired ones, although the realized left beam has not reached the desired level. Similarly, the HPBW requirement for the right beam has almost been met while that for the left beam has suffered.
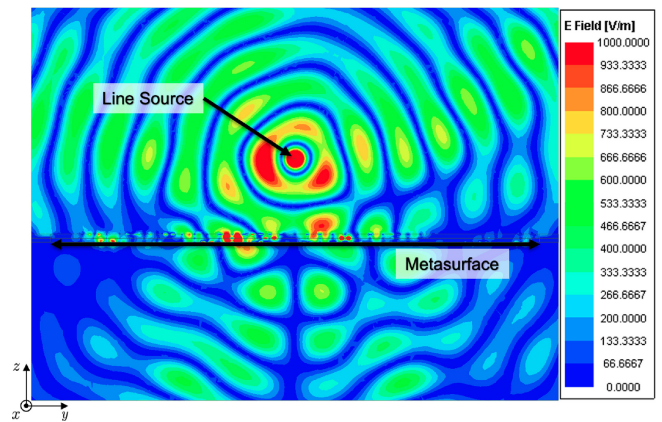

FIGURE 18. Plot of the electric field magnitude at a fixed phase. The metasurface is illuminated by a line source and then transforms this incident field to an output aperture fields in an attempt to meet the desired far-field performance criteria.

TABLE 1. Unit cell dimensions for the first design example. All dimensions are in mm.

Unit Cell Index	Top W, L	Middle W, L	Bottom W, L
#1	1.133, 1.637	2.267, 3.274	1.007, 1.322
#2	3.778, 3.841	2.833, 1.448	3.400, 3.715
#3	0.881, 3.841	2.833, 1.952	3.211, 1.826
#4	3.904, 1.763	1.322, 2.833	0.944, 3.778
#5	3.904, 2.204	2.078, 1.952	3.841, 1.322
#6	3.715, 2.141	0.881, 2.267	1.511, 2.078
#7	1.574, 2.330	3.715, 3.337	3.211, 1.700
#8	0.630, 3.022	3.904, 1.700	1.574, 2.204

Although most of the null angles have been realized, they are not as deep as required by the desired maximum null level. Also, the achieved SLL is higher than the desired one. In general, this is a difficult design task as the auxiliary surface waves required for power redistribution (in order to satisfy the LPC constraint for lossless and passive design) are heavily dependent on C_2, which was not considered when selecting the unit cells. However, noting that the reported result does not involve any fine tuning, it can be regarded as a promising initial guess. Finally, the power transmission efficiency of this metasurface was found to be 66.95%

VI. CONCLUSION

EM metasurfaces enable systematic wave transformations and can thus be utilized for the synthesis of arbitrary radiation patterns and other applications involving tailoring EM waves. The design process consists of the macroscopic and microscopic steps. Although the macroscopic design step can be made to be automated, the microscopic step can be iterative and time-consuming. To shorten the design cycle, deep learning approaches have been investigated for the microscopic design step. Herein, we have proposed an LDM-based deep learning microscopic design approach. This is based on casting multi-layered unit cell synthesis as conditional multi-channel binary image synthesis (one channel per unit cell layer). The performance of this LDM-based unit cell synthesis technique was

TABLE 2. (a) Unit cell dimensions for the second design example from unit cell #1 to #9. All dimensions are in mm. (b) Unit cell dimensions for the second design example from unit cell #10 to #31. All dimensions are in mm.

(a)

Unit Cell Index	Top W, L	Middle W, L	Bottom W, L
#1	2.267, 3.715	0.630, 1.259	2.518, 3.463
#2	0.756, 2.330	1.637, 2.455	1.259, 2.015
#3	0.693, 2.267	1.385, 3.022	2.770, 1.511
#4	1.511, 1.826	0.693, 3.022	1.322, 2.518
#5	3.337, 1.448	0.693, 2.959	1.448, 2.644
#6	1.385, 2.833	1.889, 1.952	0.944, 3.148
#7	1.700, 3.778	1.070, 1.511	3.085, 2.959
#8	0.693, 1.385	0.881, 3.463	0.630, 1.385
#9	1.448, 2.015	2.078, 2.204	1.952, 1.196

(b)

Unit Cell Index	Top W, L	Middle W, L	Bottom W, L
#10	0.630, 1.259	0.881, 1.637	1.322, 2.518
#11	3.400, 1.511	2.644, 1.385	0.944, 1.196
#12	1.385, 2.267	1.763, 1.763	1.133, 2.896
#13	2.833, 1.826	0.693, 2.959	3.274, 1.511
#14	1.259, 2.518	0.881, 2.896	1.889, 2.267
#15	1.259, 2.518	0.881, 2.896	1.889, 2.267
#16	1.889, 2.392	1.700, 2.078	0.818, 2.833
#17	1.259, 2.518	0.881, 2.896	1.889, 2.267
#18	1.259, 2.518	0.881, 2.896	1.889, 2.267
#19	2.833, 1.826	0.693, 2.959	3.274, 1.511
#20	1.385, 2.267	1.763, 1.763	1.133, 2.896
#21	3.400, 1.511	2.644, 1.385	0.944, 1.196
#22	0.630, 1.259	0.881, 1.637	1.322, 2.518
#23	1.448, 2.015	2.078, 2.204	1.952, 1.196
#24	0.693, 1.385	0.881, 3.463	0.630, 1.385
#25	1.700, 3.778	1.070, 1.511	3.085, 2.959
#26	1.385, 2.833	1.889, 1.952	0.944, 3.148
#27	3.337, 1.448	0.693, 2.959	1.448, 2.644
#28	1.511, 1.826	0.693, 3.022	1.322, 2.518
#29	0.693, 2.267	1.385, 3.022	2.770, 1.511
#30	0.756, 2.330	1.637, 2.455	1.259, 2.015
#31	2.267, 3.715	0.630, 1.259	2.518, 3.463

TABLE 3. (a) Unit cell dimensions for the third example from unit cell #1 to #23. All dimensions are in mm. (b) Unit cell dimensions for the third example from unit cell #24 to #39. All dimensions are in mm.

(a)

Unit Cell Index	Top W, L	Middle W, L	Bottom W, L
#1	1.448, 1.259	1.133, 3.904	0.944, 3.778
#2	1.826, 1.952	0.881, 3.211	1.070, 3.526
#3	1.637, 1.322	1.322, 3.778	0.881, 3.778
#4	1.133, 1.448	0.818, 3.778	1.007, 3.652
#5	0.693, 1.952	0.693, 3.841	3.463, 1.952
#6	1.007, 2.455	0.630, 3.274	2.833, 1.826
#7	3.589, 1.259	1.448, 2.392	1.070, 2.707
#8	3.589, 1.259	1.448, 2.392	1.070, 2.707
#9	0.756, 1.448	0.693, 2.959	2.518, 1.952
#10	3.337, 1.448	0.693, 2.959	1.007, 2.959
#11	0.756, 3.274	0.693, 3.085	1.322, 2.518
#12	2.959, 2.896	0.881, 1.574	1.763, 3.904
#13	0.630, 3.022	0.630, 3.463	3.841, 1.196
#14	1.574, 1.322	1.133, 3.841	0.944, 3.778
#15	3.652, 3.211	1.007, 1.259	3.022, 2.707
#16	2.015, 1.196	0.944, 3.463	0.818, 1.322
#17	3.841, 1.196	1.637, 2.581	2.959, 1.385
#18	0.630, 1.448	3.778, 1.196	0.630, 3.715
#19	1.763, 1.574	0.693, 3.148	1.007, 2.518
#20	2.078, 2.896	1.826, 3.589	0.944, 3.778
#21	0.630, 1.385	1.637, 2.455	2.770, 1.322
#22	1.070, 1.322	1.133, 3.463	3.841, 3.778
#23	1.259, 2.518	0.881, 2.896	1.889, 2.267

(b)

Unit Cell Index	Top W, L	Middle W, L	Bottom W, L
#24	0.630, 3.211	2.707, 1.448	2.015, 2.015
#25	0.944, 2.959	1.259, 2.392	2.392, 1.385
#26	1.574, 1.322	1.133, 3.841	0.944, 3.778
#27	0.881, 2.896	0.818, 3.148	2.707, 3.211
#28	3.211, 1.385	2.078, 1.322	1.826, 2.392
#29	1.196, 2.015	1.259, 3.400	0.630, 1.448
#30	2.959, 2.896	1.322, 1.259	2.204, 3.904
#31	3.085, 2.644	0.630, 1.322	2.833, 3.904
#32	1.007, 1.259	1.133, 3.022	0.881, 2.204
#33	0.944, 1.826	2.770, 1.511	1.196, 2.204
#34	1.133, 2.078	0.693, 3.337	0.881, 2.141
#35	0.756, 2.707	1.196, 2.770	2.455, 1.700
#36	0.756, 2.707	1.196, 2.770	2.455, 1.700
#37	1.574, 1.322	1.133, 3.841	0.944, 3.778
#38	0.693, 1.511	2.078, 3.085	3.841, 1.889
#39	1.448, 1.259	1.133, 3.904	0.944, 3.778

evaluated against full-wave simulations and experimental data. Although the performance of the metasurfaces formed by the unit cells generated by the LDM is not fully satisfactory, the results show that they can still provide a good initial guess for the microscopic design step.

APPENDIX

In this appendix, we have tabulated the dimensions (in mm) of the dogbones for all the unit cells used in this paper; see Tables 1–3. In particular, Tables 2 and 3 have been broken into Part A and Part B. The top layer is the closest layer to the incident wave (i.e., the input side of the metasurface) and the bottom layer is the closest layer to the generated electromagnetic wave (i.e., the output side of the metasurface).

REFERENCES

[1] C. L. Holloway, E. F. Kuester, J. A. Gordon, J. O'Hara, J. Booth, and D. R. Smith, "An overview of the theory and applications of metasurfaces: The two-dimensional equivalents of metamaterials," *IEEE Antennas Propag. Mag.*, vol. 54, no. 2, pp. 10–35, Apr. 2012.

[2] A. Epstein and G. V. Eleftheriades, "Huygens' metasurfaces via the equivalence principle: Design and applications," *J. Opt. Soc. Amer. B*, vol. 33, no. 2, pp. A31–A50, Feb. 2016.

[3] K. Achouri, M. A. Salem, and C. Caloz, "General metasurface synthesis based on susceptibility tensors," *IEEE Trans. Antennas Propag.*, vol. 63, no. 7, pp. 2977–2991, Jul. 2015.

[4] T. Brown, C. Narendra, Y. Vahabzadeh, C. Caloz, and P. Mojabi, "On the use of electromagnetic inversion for metasurface design," *IEEE Trans. Antennas Propag.*, vol. 68, no. 3, pp. 1812–1824, Mar. 2020.

[5] T. Brown, Y. Vahabzadeh, C. Caloz, and P. Mojabi, "Electromagnetic inversion with local power conservation for metasurface design," *IEEE Antennas Wireless Propag. Lett.*, vol. 19, no. 8, pp. 1291–1295, Aug. 2020.

[6] S. Pearson and S. V. Hum, "Optimization of electromagnetic metasurface parameters satisfying far-field criteria," *IEEE Trans. Antennas Propag.*, vol. 70, no. 5, pp. 3477–3488, May 2022.

[7] J. Budhu, L. Szymanski, and A. Grbic, "Design of planar and conformal, passive, lossless metasurfaces that beamform," *IEEE J. Microw.*, vol. 2, no. 3, pp. 401–418, Jul. 2022.

[8] V. G. Ataloglou, A. H. Dorrah, and G. V. Eleftheriades, "Design of compact Huygens' metasurface pairs with multiple reflections for arbitrary wave transformations," *IEEE Trans. Antennas Propag.*, vol. 68, no. 11, pp. 7382–7394, Nov. 2020.

[9] C. Niu, M. Phaneuf, T. Qiu, and P. Mojabi, "A deep learning based approach to design metasurfaces from desired far-field specifications," *IEEE Open J. Antennas Propag.*, early access.

[10] J. Ho, A. Jain, and P. Abbeel, "Denoising diffusion probabilistic models," in *Proc. Adv. Neural Inf. Process. Syst.*, vol. 33, 2020, pp. 6840–6851.

[11] C. Pfeiffer and A. Grbic, "Millimeter-wave transmitarrays for wavefront and polarization control," *IEEE Trans. Microw. Theory Techn.*, vol. 61, no. 12, pp. 4407–4417, Dec. 2013.

[12] G. Lavigne, K. Achouri, V. S. Asadchy, S. A. Tretyakov, and C. Caloz, "Susceptibility derivation and experimental demonstration of refracting metasurfaces without spurious diffraction," *IEEE Trans. Antennas Propag.*, vol. 66, no. 3, pp. 1321–1330, Mar. 2018.

[13] A. Epstein and G. V. Eleftheriades, "Arbitrary power-conserving field transformations with passive lossless omega-type bianisotropic metasurfaces," *IEEE Trans. Antennas Propag.*, vol. 64, no. 9, pp. 3880–3895, Sep. 2016.

[14] G. Xu, S. V. Hum, and G. V. Eleftheriades, "Augmented Huygens' metasurfaces employing baffles for precise control of wave transformations," *IEEE Trans. Antennas Propag.*, vol. 67, no. 11, pp. 6935–6946, Nov. 2019.

[15] V. G. Ataloglou and G. V. Eleftheriades, "Arbitrary wave transformations with Huygens' metasurfaces through surface-wave optimization," *IEEE Antennas Wireless Propag. Lett.*, vol. 20, no. 9, pp. 1750–1754, Sep. 2021.

[16] J. P. S. Wong, A. Epstein, and G. V. Eleftheriades, "Reflectionless wide-angle refracting metasurfaces," *IEEE Antennas Wireless Propag. Lett.*, vol. 15, pp. 1293–1296, 2015.

[17] A. E. Olk and D. A. Powell, "Accurate metasurface synthesis incorporating near-field coupling effects," *Phys. Rev. Appl.*, vol. 11, no. 6, 2019, Art. no. 064007.

[18] W. Liu et al., "SSD: Single shot multibox detector," in *Proc. 14th Eur. Conf. Comput. Vis. (ECCV)*, Oct. 2016, pp. 21–37.

[19] T. Wolf et al., "Transformers: State-of-the-art natural language processing," in *Proc. Conf. Empirical Methods Nat. Lang. Process. Syst. Demonstrations*, Oct. 2020, pp. 38–45. [Online]. Available: https://aclanthology.org/2020.emnlp-demos.6

[20] A. Ramesh et al., *Zero-Shot Text-to-Image Generation*, OpenAI, San Francisco, CA, USA, 2021.

[21] X. Shi, T. Qiu, J. Wang, X. Zhao, and S. Qu, "Metasurface inverse design using machine learning approaches," *J. Phys. D Appl. Phys.*, vol. 53, no. 27, 2020, Art. no. 275105.

[22] Z. Liu, D. Zhu, S. P. Rodrigues, K.-T. Lee, and W. Cai, "Generative model for the inverse design of metasurfaces," *Nano Lett.*, vol. 18, no. 10, pp. 6570–6576, Sep. 2018.

[23] F. Ghorbani, S. Beyraghi, J. Shabanpour, H. Oraizi, H. Soleimani, and M. Soleimani, "Deep neural network-based automatic metasurface design with a wide frequency range," *Sci. Rep.*, vol. 11, no. 1, pp. 1–8, 2021.

[24] M. Soltani, F. Ghorbani, S. Beyraghi, Y. Azizi, and M. Soleimani, "Multifunctional automatic metasurface design using deep learning approach." TechRxiv. Nov. 2022. [Online]. Available: https://www.techrxiv.org/articles/preprint/Multifunctional_Automatic_Metasurface_Design_Using_Deep_Learning_Approach/21507918/1

[25] J. Noh et al., "Design of a transmissive metasurface antenna using deep neural networks," *Opt. Mater. Exp.*, vol. 11, no. 7, pp. 2310–2317, Jul. 2021. [Online]. Available: https://opg.optica.org/ome/abstract.cfm?URI=ome-11-7-2310

[26] F. Wen, J. Jiang, and J. A. Fan, "Robust freeform metasurface design based on progressively growing generative networks," *ACS Photon.*, vol. 7, no. 8, pp. 2098–2104, 2020.

[27] M. Li, Y. Zhang, and Z. Ma, "Deep-learning-based metasurface design method considering near-field couplings," *IEEE J. Multiscale Multiphys. Comput. Techn.*, vol. 8, pp. 40–48, 2023.

[28] I. J. Goodfellow et al., "Generative adversarial nets," in *Proc. Adv. Neural Inf. Process. Syst.*, vol. 27, 2014, pp. 2672–2680.

[29] P. Naseri, G. Goussetis, N. J. Fonseca, and S. V. Hum, "Synthesis of multi-band reflective polarizing metasurfaces using a generative adversarial network," *Sci. Rep.*, vol. 12, no. 1, 2022, Art. no. 17006.

[30] J. A. Hodge, K. V. Mishra, and A. I. Zaghloul, "Multi-discriminator distributed generative model for multi-layer RF metasurface discovery," in *Proc. 7th IEEE Global Conf. Signal Inf. Process. (GlobalSIP)*, Jan. 2020, pp. 1–5.

[31] D. P. Kingma and M. Welling, "Auto-encoding variational Bayes," in *Proc. 2nd Int. Conf. Learn. Rep. (ICLR)*, Banff, AB, Canada, Apr. 2014, pp. 1–6.

[32] P. Naseri and S. V. Hum, "A generative machine learning-based approach for inverse design of multilayer metasurfaces," *IEEE Trans. Antennas Propag.*, vol. 69, no. 9, pp. 5725–5739, Sep. 2021.

[33] W. Ma, F. Cheng, Y. Xu, Q. Wen, and Y. Liu, "Probabilistic representation and inverse design of metamaterials based on a deep generative model with semi-supervised learning strategy," *Adv. Mater.*, vol. 31, no. 35, 2019, Art. no. 1901111.

[34] P. Naseri, S. Pearson, Z. Wang, and S. V. Hum, "A combined machine-learning/optimization-based approach for inverse design of nonuniform bianisotropic metasurfaces," *IEEE Trans. Antennas Propag.*, vol. 70, no. 7, pp. 5105–5119, Jul. 2022.

[35] S. Pearson, P. Naseri, Z. Wang, and S. V. Hum, "Applying GSTCs in electromagnetic surface inverse design using optimization and machine learning," in *Proc. IEEE Int. Symp. Antennas Propag. USNC-URSI Radio Sci. Meeting (APS/URSI)*, 2021, pp. 1511–1512.

[36] Y. Song and S. Ermon, "Generative modeling by estimating gradients of the data distribution," in *Proc. Adv. Neural Inf. Process. Syst.*, vol. 32, 2019, pp. 11895–11907.

[37] K. Achouri and C. Caloz, *Electromagnetic Metasurfaces: Theory and Applications*. Hoboken, NJ, USA: Wiley, 2021.

[38] C. Niu and P. Mojabi, "A variational auto-encoder and transformer based approach for metasurface unit cell synthesis," in *Proc. IEEE Int. Symp. Antennas Propag. USNC-URSI Radio Sci. Meeting (APS/URSI)*, 2022, pp. 1376–1377.

[39] V. G. Ataloglou et al., "Static and reconfigurable Huygens' metasurfaces: Use in antenna beamforming and beam steering," *IEEE Antennas Propag. Mag.*, vol. 64, no. 4, pp. 73–84, Aug. 2022.

[40] R. Rombach, A. Blattmann, D. Lorenz, P. Esser, and B. Ommer, "High-resolution image synthesis with latent diffusion models," in *Proc. IEEE/CVF Conf. Comput. Vis. Pattern Recognit.*, 2022, pp. 10684–10695.

[41] J. Sohl-Dickstein, E. Weiss, N. Maheswaranathan, and S. Ganguli, "Deep unsupervised learning using nonequilibrium thermodynamics," in *Proc. Int. Conf. Mach. Learn.*, 2015, pp. 2256–2265.

[42] O. Ronneberger, P. Fischer, and T. Brox, "U-Net: Convolutional networks for biomedical image segmentation," in *Proc. Int. Conf. Med. Image Comput. Comput.-Assist. Intervent.*, 2015, pp. 234–241.

[43] J. Y. Lau and S. V. Hum, "Reconfigurable transmitarray design approaches for beamforming applications," *IEEE Trans. Antennas Propag.*, vol. 60, no. 12, pp. 5679–5689, Dec. 2012.

[44] J. Budhu and A. Grbic, "Patterned unit cell design in aperiodic metasurfaces," in *Proc. 16th Int. Congr. Artif. Mater. Novel Wave Phenom. (Metamaterials)*, 2022, pp. 077–079.

[45] M. Tan and Q. Le, "EfficientNet: Rethinking model scaling for convolutional neural networks," in *Proc. 36th Int. Conf. Mach. Learn.*, vol. 97, Jun. 2019, pp. 6105–6114.

[46] N. Yu et al., "Light propagation with phase discontinuities: Generalized laws of reflection and refraction," *Science*, vol. 334, no. 6054, pp. 333–337, 2011.

[47] V. S. Asadchy, M. Albooyeh, S. N. Tcvetkova, A. Díaz-Rubio, Y. Ra'di, and S. Tretyakov, "Perfect control of reflection and refraction using spatially dispersive metasurfaces," *Phys. Rev. B, Condens. Matter, Mater. Phys.*, vol. 94, no. 7, 2016, Art. no. 75142.

[48] M. Chen, E. Abdo-Sánchez, A. Epstein, and G. V. Eleftheriades, "Theory, design, and experimental verification of a reflectionless bianisotropic Huygens' metasurface for wide-angle refraction," *Phys. Rev. B, Condens. Matter, Mater. Phys.*, vol. 97, no. 12, 2018, Art. no. 125433.

[49] M. Kelly, "Toward an end-to-end design procedure for electromagnetic Huygens' metasurfaces," M.S. thesis, Electromagnetic, Univ. Manitoba, Winnipeg, MA, Canada, 2023.

[50] D. M. Pozar, *Microwave Engineering*. Hoboken, NJ, USA: Wiley, 2005.

[51] M. Chen, A. Epstein, and G. V. Eleftheriades, "Design and experimental verification of a passive Huygens' metasurface lens for gain enhancement of frequency-scanning slotted-waveguide antennas," *IEEE Trans. Antennas Propag.*, vol. 67, no. 7, pp. 4678–4692, Jul. 2019.

[52] A. Epstein and G. V. Eleftheriades, "Synthesis of passive lossless Metasurfaces using auxiliary fields for Reflectionless beam splitting and perfect reflection," *Phys. Rev. Lett.*, vol. 117, Dec. 2016, Art. no. 256103.

[53] M. Phaneuf and P. Mojabi, "An integral equation approach to optimize surface waves for lossless and passive omega-Bianisotropic Huygens' metasurfaces," in *Proc. IEEE Int. Symp. Antennas Propag. USNC-URSI Radio Sci. Meeting (APS/URSI)*, 2022, pp. 1–2.

[54] M. Kelly, M. Phaneuf, and P. Mojabi, "A physically realizable metasurface incorporating auxiliary surface waves for power redistribution," in *Proc. 17th Eur. Conf. Antennas Propag.*, Florence, Italy, 2023, pp. 1–5.